

Entropy-Driven Design of Dual-Polymer Electrolytes for Structural Energy Storage Applications

Md Shovon Hossain, Jesse Z. Estrada-Jauregui, and Caiwei Shen*

Multifunctional electrolytes with efficient ionic transport and mechanical load-bearing are crucial for next-generation structural energy storage systems. However, existing structural electrolytes face an intrinsic trade-off between ionic conductivity and mechanical integrity. This study introduces an entropy-driven solid polymer electrolyte (SPE) design that simultaneously improves ionic transport and mechanical performance. By blending polylactic acid (PLA) and polymethyl methacrylate (PMMA) at distinct molecular weights with lithium bis(trifluoromethanesulfonyl)imide (LiTFSI), we leverage molecular-weight-mediated configurational entropy to tune SPE performance. Characterizations including differential scanning calorimetry, X-ray diffraction, and Fourier-transform infrared spectroscopy confirm miscible, interpenetrating networks with pervasive Li⁺-carbonyl coordination and high-entropy states.

Electrochemical impedance spectroscopy demonstrates all dual-polymer electrolytes outperform single-polymer counterparts in ionic conductivity. Notably, a high-entropy formulation achieves ionic conductivity three orders of magnitude higher and activation energy 50%–65% lower than single-polymer versions. Mechanically, while single-polymer electrolytes occupy opposite ends of the toughness-stiffness spectrum, dual-polymer electrolytes overcome this by combining both attributes for a balanced response. One formulation attains a synergistic balance, delivering high stiffness (≈ 0.58 GPa) while preserving substantial toughness. These results illustrate that entropy-driven tuning navigates the conductivity-mechanics trade-off, engineering SPEs with balanced properties for structural energy storage applications.

1. Introduction

In recent years, there has been a growing interest in developing advanced structural energy storage systems that can simultaneously bear mechanical loads and store electrochemical energy.^[1–3] These multifunctional materials are engineered to reduce the overall weight and volume of devices by integrating structural and electrochemical roles, which can significantly enhance both performance and device lifetime.^[4] The design and fabrication of such materials, which offer a path toward lighter, more compact, and energy-efficient devices, are therefore imperative for next-generation energy solutions.^[5,6] Much of the previous research in this area has focused on bicontinuous structural electrolytes, which are typically composed of a solid, load-bearing polymer phase, like an epoxy resin, embedded with an ion-conducting liquid phase.^[7–9] However, this approach presents significant disadvantages. The inclusion of a liquid phase, while necessary for ion transport, often compromises the mechanical integrity of the composite. Furthermore, the inert, nonconducting polymer phase can block ion access to the electrode surface, resulting in a poor electrochemical interface and a dramatic reduction in conductivity.^[10,11]

The development of single-phase solid polymer electrolytes (SPEs) represents a direct effort to overcome these shortcomings.^[12] By eliminating the separate liquid and inert phases, SPEs offer the potential for better electrochemical interfaces, improved safety over flammable liquid electrolytes,^[12–14] and seamless integration into lightweight structural composites.^[15] However, this shift reveals the more fundamental, intrinsic challenge of a trade-off between mechanical robustness and ionic conductivity. Polymers that offer high mechanical strength are typically rigid and suppress ion mobility, while those that facilitate fast ionic transport tend to be soft and lack structural integrity.^[16,17] Conventional solid or gel polymer electrolytes often reach high conductivities only through plasticization or the formation of gel networks,^[16,18–20] which softens the material and undermines its load-bearing capacity. Alternatively, strategies involving controlled hydration have shown promise. For example, the use of minor water content has been shown to boost ionic conductivity while enhancing mechanical toughness^[21] or retaining high stiffness.^[12] This success is attributed to water's preferential interaction with ions, which facilitates ion transport without significantly weakening the polymer matrix.^[22] Still intrinsically stiff polymer hosts typically provide poor ion transport.^[23] This long-standing conductivity-versus-mechanics trade-off has constrained the evolution of SPEs for applications requiring both electrochemical performance and structural integrity.

Initial attempts to navigate this trade-off led to the exploration of polymer blend electrolytes, which combine two or more polymers to achieve a synergistic balance of properties.^[24–26] For example, blending the primary ion conductor polyethylene oxide (PEO), which is mechanically soft, with a rigid, amorphous

M. S. Hossain, J. Z. Estrada-Jauregui, C. Shen
Department of Mechanical Engineering
University of Massachusetts Dartmouth
North Dartmouth, Massachusetts 02747, USA
E-mail: cshen2@umassd.edu

 Supporting information for this article is available on the WWW under <https://doi.org/10.1002/batt.202500647>

polymer like polymethyl methacrylate (PMMA) has been shown to suppress PEO crystallization, thereby improving both amorphous-phase ionic conductivity^[27,28] and mechanical strength.^[29] Similarly, other blends have been investigated to pair a polymer with high ionic conductivity with another possessing superior thermal or mechanical stability, demonstrating that a balanced performance profile is achievable through careful component selection.^[13,30–32] While promising, the inherent limitations of these binary or ternary blend systems, such as phase separation and complex interfacial dynamics, have prompted a turn toward more advanced, entropy-inspired design strategies.^[33–36] This approach, which leverages compositional complexity to create highly disordered but stable single-phase materials, was originally developed for metallic alloys and ceramics.^[37–40] This entropy-driven approach unlocks novel material systems, allowing their properties to be tailored for specific applications in energy storage, structural materials, and electronics. When extended to polymers, this strategy provides new degrees of freedom for material design. By combining multiple structurally distinct polymers with complementary functionalities, it is possible to engineer interpenetrating polymer networks (IPNs) with enhanced disorder, phase miscibility, and performance synergy across multiple axes.^[33–36,41] Although entropy stabilization has emerged as a powerful idea for materials discovery, it is rarely used to deliberately engineer functional polymer electrolytes with targeted transport and mechanical properties. Here we explore the entropy-driven design strategy for structural electrolytes using a dual-polymer electrolyte system comprising PLA, PMMA, and LiTFSI (**Figure 1**). By methodically adjusting the polymer composition and comparing at two different M_w regimes of PMMA (one below and one above the entanglement threshold),^[42] we directly modulate the system's entropic landscape. This approach allows for a systematic examination of how entropy dictates the resulting mechanical and ion transport properties, with the objective of establishing design principles for next-generation SPEs that can overcome the intrinsic trade-off between mechanical integrity and ionic performance.

2. Results and Discussion

2.1. Rationale for Material Design

In this work, the electrolyte system was systematically designed using polylactic acid (PLA), polymethyl methacrylate (PMMA), and lithium bis(trifluoromethanesulfonyl)imide (LiTFSI). PLA was selected for its favorable mechanical robustness and the presence of carbonyl groups in its ester linkages, which can facilitate ion coordination.^[21,43–45] PMMA was chosen to complement PLA due to its amorphous nature, which promotes ion mobility, and its well-established chemical compatibility with PLA.^[36,46,47] The system was doped with LiTFSI, a salt favored for its excellent thermal stability, high ionic dissociation, and the plasticizing effect of its large TFSI⁻ anion that enhances polymer segmental motion.^[48,49]

Configurational entropy plays a key role in governing compatibility and miscibility in polymer mixtures.^[50] To provide a

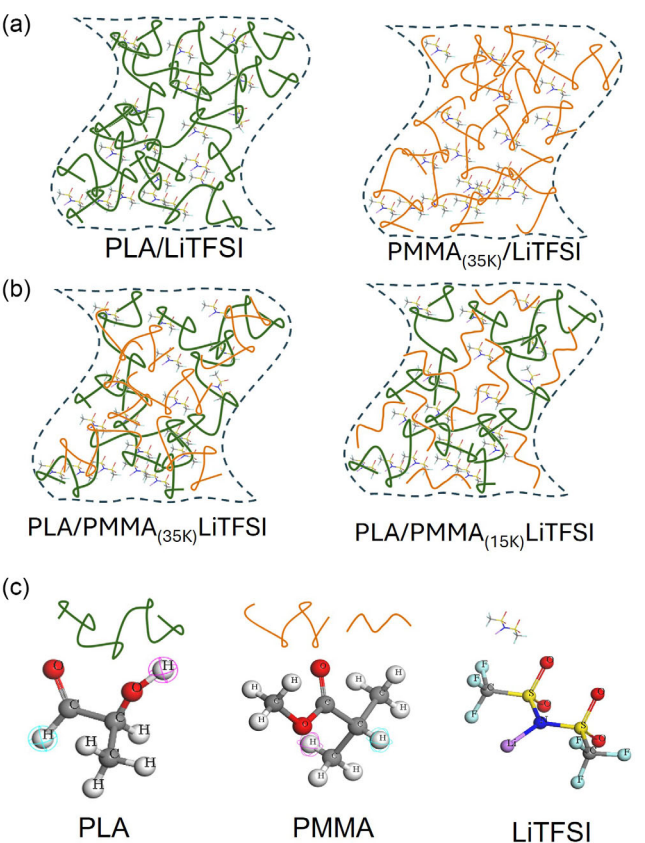


Figure 1. a) Representative images of single-polymer electrolytes comprising polylactic acid (PLA) with lithium bis(trifluoromethanesulfonyl)imide (LiTFSI), and polymethyl methacrylate (PMMA, M_w 35,000 g mol⁻¹) with LiTFSI. b) Dual-polymer electrolytes composed of PLA/PMMA_(35K)/LiTFSI and PLA/PMMA_(15K)/LiTFSI. c) Molecular structures of the constituent monomers: PLA, PMMA, and the lithium salt LiTFSI.

quantitative framework, we turn to the Flory-Huggins theory.^[51–53] It says the spontaneity of mixing depends on the Gibbs free energy of mixing (ΔG_{mix}), which reflects a balance between the enthalpic term (ΔH_{mix}) and the entropic term (ΔS_{mix}). This balance is written as

$$\Delta G_{\text{mix}} = \Delta H_{\text{mix}} - T\Delta S_{\text{mix}} \quad (1)$$

and mixing is favored when (ΔG_{mix}) is negative. To computationally assess the enthalpic component, the Flory-Huggins interaction parameter (χ) for the PLA/PMMA system was calculated using the Blends module within Materials Studio Software.^[54] Our analysis yielded a (χ) parameter of ≈ 0.08 . A small, positive (χ) value typically suggests that the mixing process is enthalpically unfavorable. However, it is critical to recognize that this computationally derived parameter primarily accounts for nonbonded interactions and does not capture the full complexity of interactions within the system, such as specific polar interactions between the carbonyl groups of PLA and PMMA.

Given these limitations of the theoretical model, experimental validation of miscibility is essential. As detailed in the Thermal Behavior and Phase Miscibility section, differential scanning calorimetry (DSC) provides this validation. The observation of a single, composition-dependent glass transition temperature (T_g) for

polymer blends (Figure S1, Supporting Information) and all dual-polymer electrolytes offers unequivocal experimental proof of molecular-level miscibility.^[55] This confirms that in the real system, the net (ΔG_{mix}) is indeed negative. Therefore, the gain in configurational entropy upon mixing must be sufficient to overcome any unfavorable enthalpic penalty and produce a stable, single-phase system.

Fundamentally, when two different polymers—such as PLA and PMMA—are mixed, the system's configurational entropy increases compared to systems containing only a single type of polymer. This increase arises from the greater number of possible ways the distinct chains can arrange themselves within the mixture. To directly quantify this critical entropic contribution, the configurational entropy of mixing (ΔS_{mix}) was calculated for each composition using the classical Flory–Huggins equation

$$\Delta S_{\text{mix}} = -R \left(\frac{\phi_{\text{PLA}}}{N_{\text{PLA}}} \ln \phi_{\text{PLA}} + \frac{\phi_{\text{PMMA}}}{N_{\text{PMMA}}} \ln \phi_{\text{PMMA}} \right) \quad (2)$$

where ϕ_{PLA} and ϕ_{PMMA} are the volume fractions, R is the gas constant, and N_{PLA} and N_{PMMA} are the degrees of polymerization for each component. This equation demonstrates that the entropy of mixing is inversely related to the degree of polymerization. Figure 2 plots the calculated (ΔS_{mix}) as a function of composition for the systems containing both 15K and 35K M_w PMMA. As the 35K and 15K M_w variants are chemically the same type of PMMA, the (χ) parameter value for the blend is expected to be the same for both series. Figure 2 clearly shows that for any given composition, the blend containing the lower-molecular-weight PMMA (15K) possesses a significantly higher configurational entropy of mixing. This larger entropic gain leads to a more favorable Gibbs free energy of mixing for the 15K M_w variants compared to their 35K M_w counterparts, providing a stronger thermodynamic driving force for miscibility and disorder.

Within this design approach, polymer molecular weight and chain entanglement also play pivotal roles. When the molecular weight exceeds the critical threshold, it promotes entanglement that influences the material's overall behavior. The critical molecular weight (M_c) marks a transition in polymer chain behavior. Below (M_c), polymer chains have little to no entanglement, resulting in enhanced segmental mobility and higher configurational

entropy. Above (M_c), chains are long enough to entangle, forming a network that increases stiffness and strength.^[56] To establish this threshold, the critical molecular weight for entanglement (M_c) of PMMA was estimated using the Synthia module,^[57] yielding a value of $\approx 20,000 \text{ g mol}^{-1}$.

2.2. Thermal Behavior and Phase Miscibility (DSC)

DSC was employed to assess the thermal transitions and miscibility of the polymer blends and their corresponding salt-containing electrolytes. The miscibility of the polymer components is crucial, as it allows for a significant increase in configurational entropy,^[50] a key principle of our high-entropy design. Figure 3 shows representative first and second heating curves for the 35K M_w and 15K M_w PMMA-based electrolytes with salt, while (Figure S1, Supporting Information) presents neat blends for 35K M_w PMMA without salt.

First-heating thermograms (Figure 3a,b) reveal a weak melting peak near 150 °C in PLA-rich compositions, corresponding to residual PLA crystallites.^[58] To eliminate prior thermal history and enthalpic relaxation, second-heating DSC runs were used to determine accurate glass-transition temperatures (T_g) of PLA/PMMA/LiTFSI electrolytes.^[59] Second-heating thermograms (Figure 3c,d) show that while single polymer electrolytes (PLA/LiTFSI and PMMA/LiTFSI) exhibit distinct T_g 's (≈ 47 and ≈ 62.5 °C, respectively), all dual-polymer electrolytes display a single, composition-dependent T_g , demonstrating molecular-level miscibility without macrophase separation.^[55,60] Neat polymer blends without the salt follow the same single T_g trend (Figure S1, Supporting Information), confirming that LiTFSI incorporation does not induce phase segregation. We note that the 15K M_w PMMA-based electrolytes generally exhibit slightly lower T_g at a given composition than the 35K M_w PMMA electrolytes, suggesting that shorter chains contribute more configurational freedom and segmental mobility.^[61] Overall, the continuous single T_g trend indicates uniform phase behavior and effective chain mixing in both M_w PMMA series, providing strong evidence that the system's stability is governed by high configurational entropy.

2.3. Structural Analysis via X-Ray Diffraction

X-ray diffraction (XRD) analysis was conducted to evaluate the crystalline behavior of both neat blends and salt-incorporated electrolytes across varying molecular weights of PMMA. Figure 4 illustrates the diffraction patterns for all salt-containing electrolytes, while (Figure S2, Supporting Information) presenting data for the corresponding neat polymer blends. Across all salt-containing samples, two broad diffraction humps centered near $2\theta = 18^\circ\text{--}20^\circ$ and $31^\circ\text{--}32^\circ$ are observed, indicative of the semicrystalline nature of PLA and the predominantly amorphous structure of PMMA.^[62,63] A notable finding is that electrolytes based on 15K M_w PMMA exhibit relatively sharper and more intense peaks in comparison to their 35K M_w PMMA counterparts, suggesting enhanced crystallinity in lower molecular weight systems.^[64] This enhanced crystallinity likely arises because PMMA

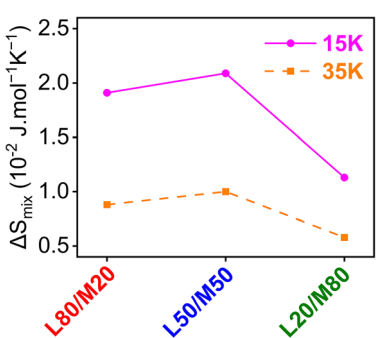


Figure 2. Calculated configurational entropy of mixing (ΔS_{mix}) for PLA/PMMA blends. The plot compares systems made with 15K M_w PMMA against those with 35K M_w PMMA at various polymer weight ratios.

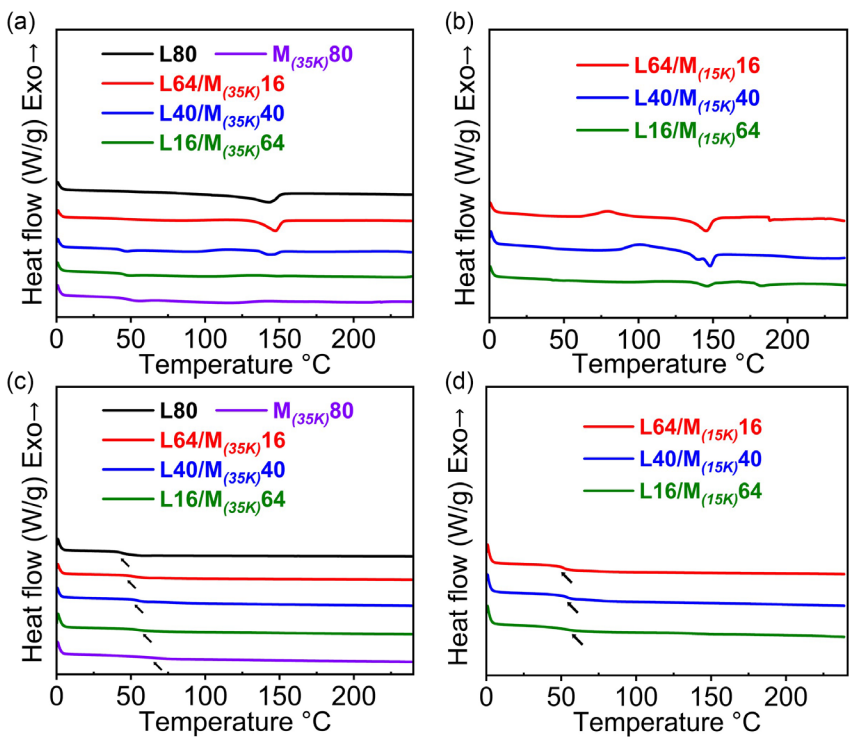


Figure 3. DSC thermograms of electrolytes. a,c) First and second heating scans, respectively, for systems containing PMMA with $M_w = 35,000 \text{ g mol}^{-1}$ ($M_{(35K)}$). b,d) Corresponding scans for systems with PMMA of $M_w = 15,000 \text{ g mol}^{-1}$ ($M_{(15K)}$). Panels (a,c) include thermograms for pure PLA (L80), pure PMMA ($M_{(35K)}80$), and PLA/PMMA mixtures L64/ $M_{(35K)}16$, L40/ $M_{(35K)}40$, and L16/ $M_{(35K)}64$. Panels (b,d) show the L64/ $M_{(15K)}16$, L40/ $M_{(15K)}40$, and L16/ $M_{(15K)}64$ compositions. Here, L and M refer to PLA and PMMA, respectively, and the numbers represent weight percentages. All samples contain 20 wt.% LiTFSI.

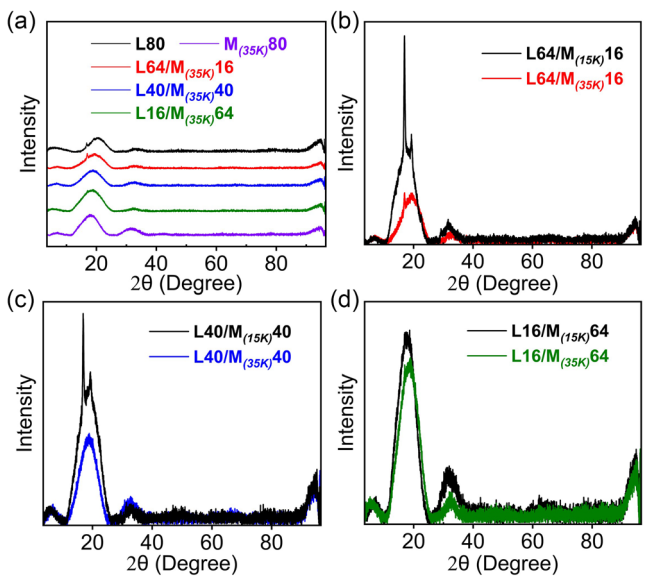


Figure 4. XRD patterns of electrolytes. a) Patterns for PLA (L80), PMMA ($M_{(35K)}$), and PLA/PMMA mixtures L64/ $M_{(35K)}16$, L40/ $M_{(35K)}40$, and L16/ $M_{(35K)}64$. b-d) Direct comparisons between ($M_{(35K)}$ - and ($M_{(15K)}$ -based counterparts at identical compositions.

below its critical molecular weight has a much lower chain entanglement density^[65] and thus higher segmental mobility and free volume. The lower entanglement density of 15K M_w PMMA allows

better chain packing, promoting local crystalline order.^[66] In contrast, electrolytes with 35K M_w PMMA exhibit broader halos and diminished peak intensities, indicative of a more amorphous structure. This reduction in crystallinity may result from restricted segmental mobility and steric hindrance due to higher chain entanglement,^[67] which impedes efficient PLA crystallization. Similar behavior has been reported in polymer blends with high M_w additives, leading to constrained phase organization.^[68]

2.4. Fourier-Transform Infrared Spectroscopy Analysis

Fourier-transform infrared (FTIR) spectroscopy was employed to investigate polymer-ion interactions and the structural evolution within the electrolytes. Spectra were obtained for both 35K and 15K molecular-weight PMMA systems across various PLA/PMMA ratios, as shown in Figure 5 and (S3, Supporting Information).

Neat PLA has characteristic peaks that represent C—O—C stretching at $1040\text{--}1220 \text{ cm}^{-1}$, C—H bending at $1350\text{--}1460 \text{ cm}^{-1}$, a prominent C=O stretching at $\approx 1750 \text{ cm}^{-1}$, and —CH stretching at $2850\text{--}2920 \text{ cm}^{-1}$. For PMMA, major absorptions include —CH stretching around $2945\text{--}2995 \text{ cm}^{-1}$ and a strong C=O stretch near 1723 cm^{-1} .^[69] PMMA also exhibits C—H deformation bands at $1385\text{--}1480 \text{ cm}^{-1}$, and asymmetric C—O—C stretching near $1060\text{--}1270 \text{ cm}^{-1}$.^[70] Both 15K and 35K M_w PMMA show almost identical band positions, reflecting their common chemical structure. The bis(trifluoromethanesulfonyl)imide anion of the LiTFSI

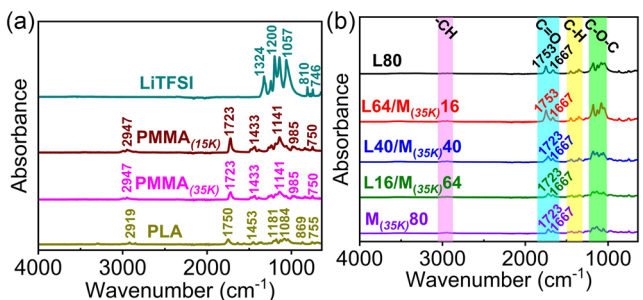


Figure 5. FTIR spectra of a) pure components (PLA, PMMA_(35K), PMMA_(15K), and LiTFSI) and b) electrolytes (L80, M_(35K)80, L64/M_(35K)16, L40/M_(35K)40, and L16/M_(35K)64).

salt has distinctive IR bands. Asymmetric S=O stretches appear around 1324 cm⁻¹. A sharp S—N—S asymmetric stretching mode occurs near 1057 cm⁻¹ and peaks at 810 and 746 cm⁻¹ are assigned to symmetric S—N—S stretching and CF₃ bending, respectively. Peaks at 1200 and 1142 cm⁻¹ are assigned to the CF₃ symmetric stretching mode and combination of C—SO₂—N bonding and C—F stretching mode, respectively.^[71]

In all electrolytes, the broad aliphatic —CH stretching peaks persist. Each spectrum shows bands at 2995 and 2950 cm⁻¹. These arise from —CH groups in PLA/PMMA, and for L80 composition, it shifts from 2850 to 2920 cm⁻¹ with the addition of salt. The carbonyl C=O band is a key probe of polymer-Li⁺ interaction. In single-polymer electrolytes, L80 shows C=O peak near 1753 cm⁻¹, consistent with the 1750 cm⁻¹ value for neat PLA. PMMA/LiTFSI shows its primary C=O peak at 1723 cm⁻¹. In dual-polymer electrolytes, the carbonyl peak position reflects each polymer's contribution. For example, L64/M_(35K)16 still has a 1753 cm⁻¹ peak plus a shoulder at ≈1667 cm⁻¹. In PMMA-rich electrolytes, the main C=O peak shifts fully to ≈1723 cm⁻¹. Notably, all the electrolytes show additional low-frequency shoulders at ≈1667 cm⁻¹, flanking the main C=O peak. These sub-1750 cm⁻¹ features are absent in neat polymers and likely indicate Li⁺-coordination to carbonyl oxygens.^[72] This coordination weakens the C=O double bond, inducing a redshift to a lower wavenumber. Thus, each electrolyte shows two carbonyl bands: a free C=O (1753 or 1723 cm⁻¹) and a Li-bound C=O at lower wavenumber (≈1667 cm⁻¹). To quantify the extent of this crucial polymer-ion coordination, the carbonyl stretching region (1800–1600 cm⁻¹) of each electrolyte spectrum was deconvoluted into its constituent peaks.^[73] This analysis isolates contributions from free PLA C=O, free PMMA C=O, and a common Li⁺-coordinated C=O peak, as shown for all compositions in Figure S4, Supporting Information. The relative percentages of free and Li⁺-bound carbonyl populations, determined from the integrated areas of these deconvoluted peaks, are summarized in **Table 1**.

Other regions of the spectra provide further structural information. The 1350–1480 cm⁻¹ region is dominated by C—H deformation modes. The exact positions and intensities of the peaks vary slightly with PLA/PMMA content and generally match the known PLA/PMMA fingerprint. C—O—C stretches and other

Table 1. Relative percentages of free and Li⁺-bounded carbonyl (C=O) groups for various samples.

Electrolytes	Free C=O [%]	Li ⁺ -bounded C=O [%]
L80	67.4	32.6
M _(35K) 80	60.45	39.55
L64/M _(35K) 16	75.99	24.01
L40/M _(35K) 40	71.26	28.74
L16/M _(35K) 64	64.19	35.81
L64/M _(15K) 16	69.63	30.37
L40/M _(15K) 40	55.4	44.6
L16/M _(15K) 64	65.29	34.71

backbone vibrations lie in the 1040–1270 cm⁻¹ region. PLA has C—O—C near 1084 cm⁻¹ and PMMA has an asymmetric C—O—C mode around 1141 cm⁻¹. The speciation of the TFSI⁻ anion was also investigated. However, key vibrational modes of the anion that are sensitive to ion pairing, such as the S—N—S stretch (≈1057 cm⁻¹) and the S=O stretch (≈1324 cm⁻¹), are located in regions with significant spectral overlap from the strong, broad absorption bands of the PLA and PMMA polymer backbones. Due to this heavy spectral congestion, it is challenging to reliably deconvolve or distinguish the subtle changes in the TFSI⁻ bands that would be required for a quantitative analysis of ion pairing. Nevertheless, a qualitative inspection of the spectra does not reveal the emergence of any distinct new peaks in the 760–790 cm⁻¹ range, which are characteristic of significant contact ion pair formation.^[74] Finally, variation in PMMA molecular weight from 35K to 15K exerts a negligible effect on FTIR band positions, affecting only the relative peak intensities (Figure S3, Supporting Information).

2.5. Ionic Conductivity

Electrochemical impedance spectroscopy (EIS) was employed to investigate ionic transport behavior across the temperature range of 20–120 °C. As shown in **Figure 6a,b**, all samples exhibit thermally activated conductivity.

A key finding is that every dual-polymer electrolyte (PLA/PMMA/LiTFSI) exhibited higher ionic conductivity than its single-polymer counterparts. At 20 °C, for instance, the single-polymer electrolyte systems of PLA with lithium salt (L80) and PMMA with lithium salt (M_(35K)80) show ionic conductivities of ≈1.13 × 10⁻¹¹ and 2.06 × 10⁻¹¹ S cm⁻¹, respectively. In contrast, all three 35K M_w PMMA-based electrolytes (L64/M_(35K)16, L40/M_(35K)40, and L16/M_(35K)64) demonstrate enhanced performance, with ionic conductivities of ≈5.33 × 10⁻¹¹, 8.02 × 10⁻¹¹, and 1.55 × 10⁻⁹ S cm⁻¹, respectively. The 15K M_w PMMA-based electrolytes demonstrated even greater enhancements, with conductivities of 1.04 × 10⁻¹⁰ S cm⁻¹ for L64/M_(15K)16, 2.04 × 10⁻⁹ S cm⁻¹ for L40/M_(15K)40, and 8.69 × 10⁻⁸ S cm⁻¹ for L16/M_(15K)64. The L16/M_(15K)64 composition stood out, exhibiting the highest ionic conductivity at 20 °C, a trend that remains consistent across elevated temperatures.

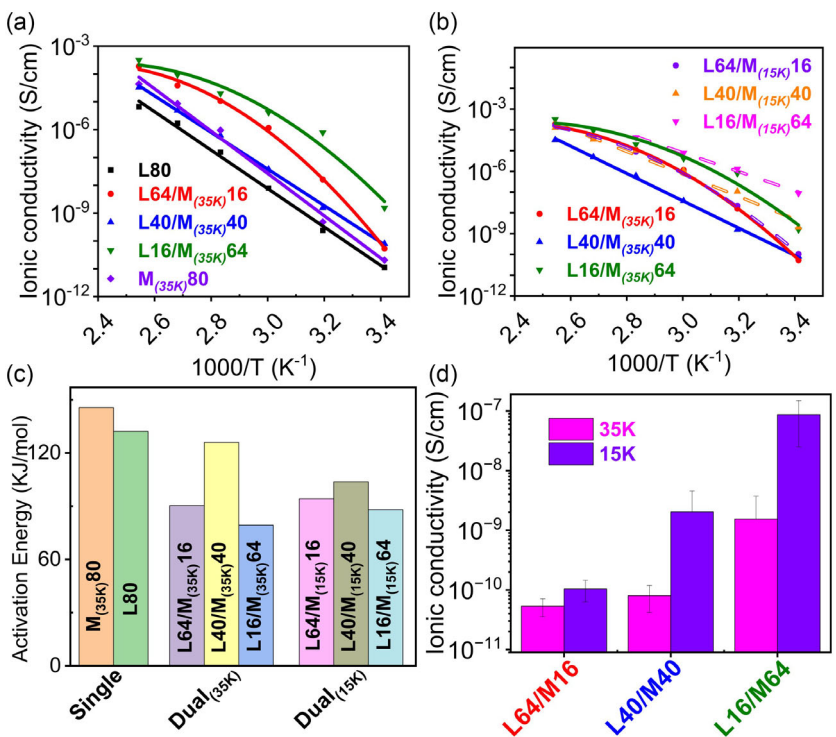


Figure 6. a) Ionic conductivity plots ($\ln\sigma$ vs. $1000/T$) measured at five temperature points (20–120 °C) for the single-polymer electrolytes and 35K M_w PMMA-based electrolytes. b) Ionic conductivity plots comparing the 35K M_w PMMA-based electrolytes and 15K M_w PMMA-based electrolytes. c) Activation energies (E_a) extracted from linear fits to the data in (a,b) for all compositions. d) Direct comparison of ionic conductivity at 20 °C between each 35K PMMA-based electrolytes and its corresponding 15K variants.

The temperature-dependent conductivity plots offer deeper insight into the transport mechanism. Three specific dual-polymer systems, namely, the 35K-based L64/M16 and L16/M64 along with the 15K-based L64/M16, exhibit the distinct curvature characteristic of Vogel-Tamman-Fulcher (VTF) behavior at lower temperatures.^[75,76] This behavior indicates that ion mobility is strongly coupled to the segmental motion of the polymer chains below the material's glass transition temperature. At elevated temperatures, however, the profiles for these compositions tend toward linearity. The remaining compositions displayed a linear, Arrhenius-type behavior across the entire temperature range.^[77] This transition from VTF to linear behavior suggests that the transport mechanism becomes decoupled from large-scale segmental motion.^[78] Instead, it is dominated by localized ion hopping between adjacent coordination sites, a process well described by the Arrhenius relationship. The activation energies (E_a) were calculated based on these distinct behaviors. For the three compositions showing curved VTF behavior, a linear fit was applied to the high-temperature region above the glass transition temperature where the Arrhenius process is dominant. For all other compositions, the activation energy was obtained from a linear fit across the full temperature range.

Analysis of the activation energies reveals a complex relationship with the system's configurational entropy of mixing (ΔS_{mix}). Although all dual-polymer electrolytes have a lower activation energy than their single-polymer counterparts, the trends within the blended systems are not monotonic. The calculated

configurational entropy is highest for the 1:1 compositions and is consistently greater for the 15K M_w systems compared to the 35K M_w systems (Figure 2). The activation energy trends, however, do not simply follow the inverse of the entropy. The L40/M40 compositions exhibit the highest activation energy within their respective series. Furthermore, the comparison between molecular weights is nuanced. For the L40/M40 composition, the 35K system shows a higher activation energy than the 15K system. Conversely, for the other two compositions, the 15K systems have slightly higher activation energies than their 35K counterparts. This complex behavior suggests that high configurational entropy is crucial but its influence is modulated by local effects related to chain entanglement. At the L40/M40 composition, where entropy is maximized, the high chain entanglement of the 35 K system may compound the disorder, creating more significant kinetic traps for Li⁺ ions^[79] and thus a higher activation energy. In the other compositions, where one polymer dominates, the effect of local chain packing may be more significant. Here, the lower entanglement of the 15 K chains could allow for more ordered local packing, establishing slightly more defined and higher energy barriers compared to the more amorphous 35K systems Figure 4.

To quantitatively probe the mechanism driving this conductivity enhancement, we deconvoluted the carbonyl (C=O) stretching region of the FTIR spectra. This allowed us to determine the percentage of Li⁺-bound carbonyl groups and correlate the results with ionic conductivity, as shown in the Figure 7. This analysis uncovered a complex, nonmonotonic relationship that

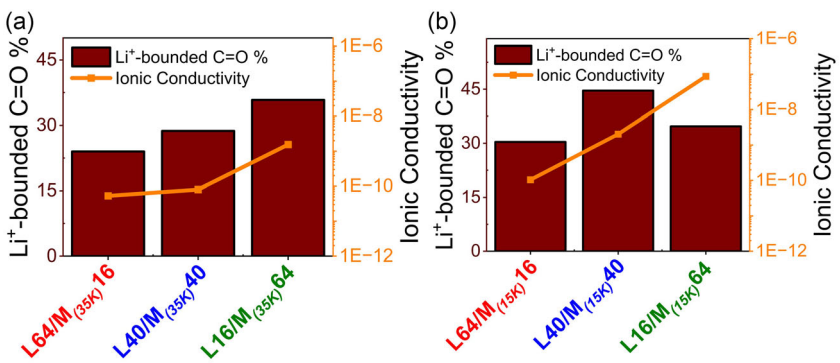


Figure 7. Quantitative correlation between Li^+ -carbonyl coordination and ionic conductivity. The percentage of Li^+ -bound carbonyl ($\text{C}=\text{O}$) groups, as determined from the deconvolution of FTIR spectra (bar graphs, left axis), is plotted against the measured ionic conductivity at 20 °C (line plots, right axis) for dual-polymer electrolytes. The comparison is shown for systems containing a) 35K M_w PMMA and b) 15K M_w PMMA.

provides deeper insight into the ion transport mechanism. For instance, in the 35K M_w PMMA series, conductivity generally increases with the percentage of Li^+ -bound carbonyls, peaking at 35.8% for the most conductive L16/M_(35K)64 sample. The 15K M_w series, however, displays a more nuanced trend. The L40/M_(15K)40 composition shows the highest fraction of Li^+ -bound carbonyls at 44.6%. Despite this, its ionic conductivity is lower than that of the L16/M_(15K)64 sample, which has a smaller bound carbonyl fraction of 34.7%. This finding highlights the well-established trade-off between carrier generation and ion mobility in polymer electrolytes.^[80] A high degree of Li^+ -polymer coordination is essential for salt dissociation and increasing the number of mobile charge carriers. However, excessive or overly strong coordination can immobilize the Li^+ ions, which reduces their mobility and hinders overall transport.^[80] The L40/M_(15K)40 system appears to be a case of such overcoordination, where the benefit of a high carrier concentration is outweighed by reduced Li^+ mobility. In contrast, the L16/M_(15K)64 composition achieves a more optimal balance. It provides sufficient coordination for effective salt dissociation while maintaining more facile pathways for ion hopping. This result demonstrates that the entropy-driven design allows for fine-tuning the coordination environment to achieve an optimal state that maximizes ionic conductivity.

The superior performance of electrolytes based on lower M_w PMMA (15K) clearly manifests the principles of the entropy-driven design (Figure 6). Using shorter polymer chains lowers system viscosity, increases the number of chain ends,^[81] and amplifies the entropic effect through enhanced molecular diversity. This leads to higher overall conductivities compared to their corresponding 35K compositions. The general reduction in activation energy seen in dual-polymer systems, relative to their single-polymer counterparts, also stems from this design. In a single-polymer system, Li^+ ions occupy a narrow distribution of coordination sites with well-defined energies. This requires them to overcome a significant and uniform activation barrier. In the high-entropy dual-polymer systems, configurational disorder creates many unique local chemical environments, which results in a broad, statistical distribution of Li^+ site energies.^[82–84] This varied energetic landscape fosters the formation of low-energy

transport pathways. However, the main reason for the enhanced conductivity in the 15K systems appears to be the exponential increase in accessible hopping sites. This entropic effect vastly increases the Arrhenius prefactor (σ_0),^[85] which is proportional to both the number of charge carriers and available sites. The substantial gain in this prefactor more than compensates for the slightly higher activation energies in the 15K systems, resulting in a net increase in overall ionic conductivity. High-entropy design, already used in liquid electrolytes to disrupt ion-solvent coordination and boost Li^+ diffusivity,^[86] similarly imparts pronounced conductivity enhancements when translated to solid polymer matrices.

Thus, the strategic use of a high-entropy design framework provides nuanced control over the competing factors of ion coordination, polymer segmental dynamics, and the energetic landscape. This approach ultimately yields substantially enhanced ionic conductivity in these dual-polymer systems.

2.6. Mechanical Properties

The tensile behavior of both the high-entropy polymer blends (Figure S5 and S6, Supporting Information) and electrolytes was evaluated to understand the effect of entropy and critical molecular weight on mechanical properties relevant for structural energy storage. Figure 8 presents the stress-strain profiles and derived mechanical parameters for high-entropy electrolytes. L80 shows very high elongation ($\approx 209\%$) and toughness ($\approx 13 \text{ MJ m}^{-3}$) but low stiffness ($\approx 0.11 \text{ GPa}$) and moderate strength ($\approx 9 \text{ MPa}$). In contrast, PMMA-rich compositions are stiff and strong but brittle. For example, the M_(35K)80 sample has a comparatively high Young's modulus ($\approx 0.50 \text{ GPa}$) but fractures at $<1\%$ elongation, with negligible toughness. Mixing PLA, PMMA, and LiTFSI to form high-entropy SPEs resulted in notable synergistic effects. Evidently, L64/M_(35K)16 electrolyte reaches the highest modulus ($\approx 0.58 \text{ GPa}$) while retaining large ductility ($>216\%$ elongation) and high toughness ($\approx 9.9 \text{ MJ m}^{-3}$). Such simultaneous enhancement of stiffness and ductility arises from the PLA/PMMA/LiTFSI electrolyte's elevated configurational entropy, which drives entropy-favored mixing and yields a cohesive nanoscale network that both sustains

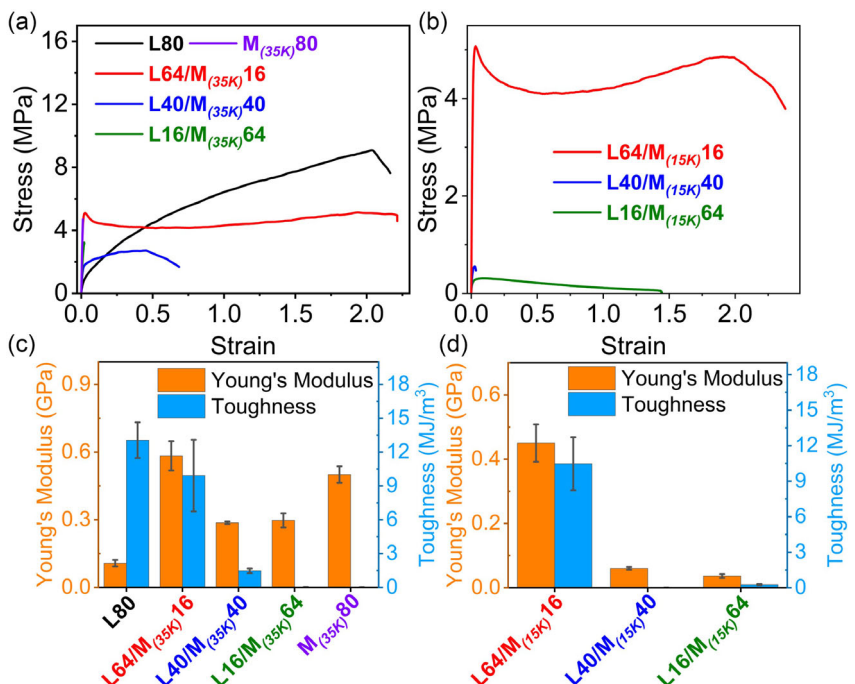


Figure 8. a) Tensile stress–strain curves for the single-polymer electrolytes and 35K M_w PMMA-based electrolytes. b) Tensile stress–strain curves for the 15K M_w PMMA-based electrolytes. c) Bar chart summarizing Young's modulus and toughness (area under the stress–strain curve) for the compositions in panel (a). d) Bar chart of Young's modulus and toughness for the compositions in panel (b).

mechanical load and dissipates energy through chain-level dynamics.^[36,41,87,88] Critical molecular weight also strongly influences the electrolyte mechanics. The 35K M_w PMMA-based electrolytes yield much higher stiffness and strength than the 15K M_w PMMA series. For example, the L64/M16 electrolyte has $E \approx 0.58$ GPa for 35K M_w vs. 0.45 GPa for 15K M_w , and both maintain high elongation ($\approx 217\%–229\%$). In other compositions, the differences are dramatic: the L40/M_(15K)40 electrolyte is extremely weak ($E \approx 0.06$ GPa, tensile strength ≈ 0.56 MPa) compared to $E \approx 0.29$ GPa for 35K M_w , with elongation dropping from $\approx 60\%$ to $\approx 3\%$. However, the unusually high elongation of L16/M_(15K)64 arises from the low entanglement density of 15K M_w PMMA, which permits extensive chain mobility,^[56,66,89,90] and from LiTFSI-induced plasticization,^[91] together enabling greater ductility compared to the stiffer, more constrained 35K M_w counterpart. These trends reflect the role of chain entanglements, because once molecular weight exceeds the critical molecular weight, a physical network forms that enhances modulus and strength.^[56,66,92] Below this critical molecular weight, chains slip easily, and the material softens dramatically.

Our findings echo broader trends in high-entropy polymeric and electrolyte materials, where increasing configurational entropy through multicomponent design leads to morphology stabilization and simultaneous enhancement of mechanical robustness and functional performance.^[35] For instance, recent work on high-entropy tape electrolytes demonstrated that leveraging polymer–ion interactions in conjunction with increased configurational entropy leads to the formation of stable microstructures with liquid-like ion conduction. This entropy-engineered design produced cohesive polymer networks with markedly enhanced

mechanical performance, including high elongation, strong tape-like interfacial adhesion, and mechanical robustness, as evidenced by toughness values of 11.28 ± 1.12 MJ m⁻³ and tensile strength of 8.18 ± 0.28 MPa.^[33] Another study reports the development of high-entropy microdomain interlocking all-solid-state polymer electrolytes by incorporating multifunctional ABC miktoarm star terpolymers into a polyethylene oxide matrix. This design facilitates the formation of hierarchical micro- and nano-scale dynamic interlocking networks characterized by high topological structure entropy. As a result, the polymer electrolytes exhibit excellent mechanical toughness, significant ionic conductivity, and a high lithium-ion transference number of 0.63.^[34] By leveraging these entropy-driven supramolecular networks, the system effectively reconciles mechanical robustness with fast ion transport—offering a promising pathway for high-performance solid-state battery chemistries. These studies highlight that elevated configurational entropy not only improves ionic homogeneity but also facilitates energy dissipation and load-bearing ability via chain-level mixing and entanglement networks.

3. Conclusion

In conclusion, this work demonstrates that a high-entropy design approach achieved by mixing PLA and PMMA across critical molecular-weight thresholds in the presence of LiTFSI offers a compelling solution to the inherent trade-off between ionic conductivity and mechanical robustness in SPEs. By carefully tuning configurational entropy through both compositional diversity

and molecular weight selection, the resulting IPNs present single-phase behavior, enhanced Li⁺ coordination, and notable improvements in both ionic transport and structural performance. High-entropy electrolytes, especially those containing lower-molecular-weight PMMA, deliver ionic conductivity several orders of magnitude higher and substantially lower activation energies compared to single-polymer counterparts, while optimized high-molecular-weight formulations retain mechanical stiffness and toughness necessary for load-bearing applications. These findings underscore the potential of entropy-guided polymer mixing as a rigorous and versatile strategy for engineering advanced SPEs tailored to the functional and structural demands of next-generation energy storage systems.

4. Experimental Section

Materials

Polylactic acid (PLA, 2003D), with a weight-average molecular weight (M_w) of 110,000 g mol⁻¹, was purchased from 3devo. Polymethyl methacrylate (PMMA) with two distinct weight-average molecular weights ($M_w = 15,000$ g mol⁻¹ and $M_w = 35,000$ g mol⁻¹) were procured from Sigma-Aldrich. Lithium bis(trifluoromethanesulfonyl)imide (LiTFSI, battery grade, >99.9%) and the solvent, N,N-dimethylformamide (DMF, anhydrous, ≥99.8%), were also purchased from Sigma-Aldrich. To prevent moisture uptake, all materials were stored in a dry environment and used as received without any further drying.

Preparation of Polymer Electrolyte Films

Both neat polymer blends and salt-containing electrolytes were fabricated via a solution casting method. For the electrolyte samples, the total polymer content (PLA + PMMA) was fixed at 80 wt.%, with the remaining 20 wt.% being LiTFSI. For a typical batch, the predetermined amounts of PLA, PMMA, and LiTFSI, detailed in **Table 2**, were dissolved in DMF to form a solution. The mixture was stirred magnetically on a hot plate at 110 °C for 24 h inside a fume hood to ensure the formation of a visually clear, homogeneous solution. The resulting solution was cast into a flat-bottomed PTFE Petri dish and heated on a hot plate at 110 °C for an additional 24 h to evaporate the bulk of the solvent. To ensure complete removal of any residual DMF, the resulting free-standing films were then transferred to an oven and dried at 155 °C for 3 h. The final electrolyte films were then ready to be processed for different characterizations. Neat polymer blends (without LiTFSI) were prepared following the same procedure.

DSC Test

To evaluate the phase transition temperatures of samples, DSC was conducted on a TA Instruments DSC25. Dried electrolyte samples weighing 5–10 mg were prepared and carefully placed into Tzero aluminum pans for analysis within the controlled environment of a glovebox. The samples were subjected to a heat/cool/heat/cool cycle under a nitrogen atmosphere (50 mL min⁻¹). The analysis began by equilibrating the sample at 0 °C, followed by heating to 240 °C at a rate of 10 °C min⁻¹. The temperature was then held to achieve equilibrium at 240 °C before being cooled back down to 0 °C. After another equilibrium held at 0 °C, a second heating scan was run to 240 °C, followed by a final cooling step back down to 0 °C. The first cycle served to erase the sample's thermal history, and the second heating scan was used for T_g calculations. The glass transition temperature (T_g) was determined as the midpoint of the step change in heat capacity.

XRD Test

XRD was employed to analyze the crystallinity of the materials using a Bruker D8 Discovery Diffractometer, scanning from 5° to 95° at a controlled speed. The samples tested included PLA, PMMA, PLA/PMMA blends, and dried polymer electrolytes. For preparation, small amounts of the dried polymer electrolyte, as well as PLA, PMMA, and blends, were collected. The polymer electrolyte films were carefully cut into smaller pieces and mounted on glass slides and then securely sealed with Kapton tape to maintain positioning. All sample handling took place in a dry, controlled glovebox atmosphere, minimizing exposure to moisture and ensuring the accuracy of the measurements.

Electrochemical Testing

All electrochemical measurements were conducted using a Gamry Reference 600 potentiostat. The ionic conductivity of the SPE membranes was evaluated via EIS over a frequency range of .01 Hz to 1 MHz at different temperatures. Prior to testing, the electrolyte membranes were prepared using a hot rolling process to ensure uniform thickness and minimize variability in measurements. The ionic conductivity (σ) was calculated using the following formula

$$\sigma = \frac{d}{R_b \times A} \quad (3)$$

where σ is the ionic conductivity (S cm⁻¹), d is the thickness of the membrane (cm), R_b is the bulk resistance obtained from the

Table 2. Weight percentages of PLA, PMMA, and LiTFSI in each electrolyte formulation.

Electrolytes	PLA [wt.%]	PMMA _(15K) [wt.%]	PMMA _(35K) [wt.%]	LiTFSI [wt.%]
L80	80	0	0	20
M80 _(35K)	0	0	80	20
L64/M _(35K) 16	64	0	16	20
L40/M _(35K) 40	40	0	40	20
L16/M _(35K) 64	16	0	64	20
L64/M _(15K) 16	64	16	0	20
L40/M _(15K) 40	40	40	0	20
L16/M _(15K) 64	16	64	0	20

Nyquist plot (Ω), and A is the electrode–electrolyte interfacial area (cm^2). Care was taken to ensure proper contact between the membrane and stainless-steel blocking electrodes to reduce contact resistance and obtain accurate impedance data.

Mechanical Testing

The mechanical properties of the prepared structural polymer electrolytes were evaluated using a universal testing machine (Instron 3345, 5 KN load cell) in accordance with ASTM D882, which is the standard method for tensile testing of thin plastic films. Samples were elongated at a constant crosshead speed of 5 mm min^{-1} under ambient conditions. To ensure uniform sample geometry and thickness, the electrolyte membranes were first processed using an MTI MSK-HRP-1A hot rolling machine to achieve a consistent thickness of $\approx 0.5 \text{ mm}$. Subsequently, the rolled membranes were trimmed to standardized dimensions of $\approx 100 \text{ mm}$ in length and 15 mm in width. Mechanical tests were performed immediately after trimming, without further conditioning. Each composition was tested 4–5 times to ensure reproducibility, and all measurements were conducted at room temperature.

Acknowledgements

The work is supported by the National Science Foundation grant 2217172, the UMass Dartmouth’s Marine and Undersea Technology (MUST) Research Programs funded by the Office of Naval Research (ONR) under grant numbers N00014-20-1-2170 and N00014-25-1-2315, and the UMass Dartmouth’s MultiSEED Award.

Conflict of Interest

The authors declare no conflict of interest.

Data Availability Statement

The data that support the findings of this study are available from the corresponding author upon reasonable request.

Keywords: critical molecular weight • high-entropy design • polymer electrolyte • structural energy storage

- [1] A. M. Navarro-Suárez, M. S. P. Shaffer, *Front. Chem.* **2021**, *9*, 810781.
- [2] M. A. Raja, W. Kim, W. Kim, S. H. Lim, S. S. Kim, *ACS Appl. Mater. Interfaces* **2025**, *17*, 20125.
- [3] M. A. Raja, S. H. Lim, D. Jeon, S. Bae, W. Oh, I. Yang, D. Kang, J. Ha, H. E. Lee, I. K. Oh, S. Kim, S. S. Kim, *ACS Appl. Mater. Interfaces* **2024**, *16*, 59128.
- [4] M. S. Siraj, S. Tasneem, D. Carlstedt, S. Duan, M. Johansen, C. Larsson, J. Xu, F. Liu, F. Edgren, L. E. Asp, *Adv. Energy Sustainability Res.* **2023**, *4*, 2300109.
- [5] F. Danzi, R. M. Salgado, J. E. Oliveira, A. Arteiro, P. P. Camanho, M. H. Braga, *Molecules* **2021**, *26*, 2203.
- [6] X. Wu, A. Chen, X. Yu, Z. Tian, H. Li, Y. Jiang, J. Xu, *ACS Nano* **2024**, *18*, 20957.
- [7] B. K. Muñoz, A. del Bosque, M. Sánchez, V. Utrilla, S. G. Prolongo, M. G. Prolongo, A. Ureña, *Polymer (Guildf.)* **2021**, *214*, 123233.
- [8] J. Y. Lim, D. A. Kang, N. U. Kim, J. M. Lee, J. H. Kim, *J. Membr. Sci.* **2019**, *589*, 117250.
- [9] A. S. Westover, B. Baer, B. H. Bello, H. Sun, L. Oakes, L. M. Bellan, C. L. Pint, *J. Mater. Chem. A Mater.* **2015**, *3*, 20097.
- [10] N. Shirshova, A. Bismarck, S. Carreyette, Q. P. V. Fontana, E. S. Greenhalgh, P. Jacobsson, P. Johansson, M. J. Marczewski, G. Kalinka, A. R. J. Kucernak, J. Scheers, M. S. P. Shaffer, J. H. G. Steinke, M. Wienrich, *J. Mater. Chem. A Mater.* **2013**, *1*, 15300.
- [11] W. Johannesson, D. Zenkert, G. Lindbergh, R. Pejman, E. Caglan Kumbur, A. Raeisi Najafi, V. Tu, L. E. Asp, N. Shirshova, F. Larsson, K. Runesson, Jänicke R., *Multifunct. Mater.* **2020**, *3*, 025001.
- [12] N. Joyal, Y. C. Chang, M. Shonar, V. Chalivendra, C. Shen, *J. Energy Storage* **2022**, *51*, 104459.
- [13] L. P. Teo, M. H. Buraidah, A. K. Arof, *Molecules* **2021**, *26*, 6499.
- [14] W. Wang, S. Guo, F. Feng, Q. Li, H. Cai, A. Rougier, D. Ma, J. Wang, *Polym. Rev.* **2025**, *65*, 302.
- [15] Y. Fu, Y. Chen, X. Yu, L. Zhou, *Compos. Sci. Technol.* **2022**, *230*, 109731.
- [16] Q. Zhao, S. Stalin, C. Z. Zhao, L. A. Archer, *Nat. Rev. Mater.* **2020**, *5*, 229.
- [17] J. Mindemark, M. J. Lacey, T. Bowden, D. Brandell, *Prog. Polym. Sci.* **2018**, *81*, 114.
- [18] S. B. Aziz, T. J. Woo, M. F. Z. Kadir, H. M. Ahmed, *J. Sci.: Adv. Mater. Devices* **2018**, *3*, 1.
- [19] Y. Wang, W. H. Zhong, *ChemElectroChem* **2015**, *2*, 22.
- [20] K. S. Ngai, S. Ramesh, K. Ramesh, J. C. Juan, *Ionics (Kiel)* **2016**, *22*, 1259.
- [21] Y. C. Chang, P. Teymoory, C. Shen, *Adv. Mater. Technol.* **2024**, *9*, 2400033.
- [22] A. S. Asha, M. Jamal, S. Gravelle, M. L. Mayes, C. Shen, *J. Phys. Chem. B.* **2025**, *129*, 1061.
- [23] Z. Xue, D. He, X. Xie, *J. Mater. Chem. A Mater.* **2015**, *3*, 19218.
- [24] N. Yazie, D. Worku, N. Gabbiye, A. Alemanyehu, Z. Getahun, M. Dagnew, *Mater. Renewable Sustainable Energy* **2023**, *12*, 73.
- [25] B. Oh, Y. R. Kim, *Solid State Ion* **1999**, *124*, 83.
- [26] M. P. Blatt, D. T. Hallinan, *Ind. Eng. Chem. Res.* **2021**, *60*, 17303.
- [27] K. P. Sindhu, S. S. M. A. Majed, J. S. Parveen, *J. Electron. Mater.* **2021**, *50*, 6654.
- [28] R. Bakar, S. Darvishi, T. Li, M. Han, U. Aydemir, S. Nizamoglu, K. Hong, E. Senses, *ACS Appl. Polym. Mater.* **2022**, *4*, 179.
- [29] M. S. Khan, S. Sultana, *Int. J. Polym. Sci.* **2015**, *2015*, 101692.
- [30] E. E. Ushaková, A. V. Sergeev, A. Morzhukhin, F. S. Napol'skiy, O. Kristavchuk, A. V. Chertovich, L. V. Yashina, D. M. Itkis, *RSC Adv.* **2020**, *10*, 16118.
- [31] L. N. Sim, S. R. Majid, A. K. Arof, *Vib. Spectrosc.* **2012**, *58*, 57.
- [32] J. Yan, W. Huang, T. Hu, H. Huang, C. Zhu, Z. Chen, X. Fan, Q. Wu, Y. Li, *Molecules* **2025**, *30*, 2422.
- [33] X. He, Z. Zhu, G. Wen, S. Lv, S. Yang, T. Hu, Z. Cao, Y. Ji, X. Fu, W. Yang, Y. Wang, *Adv. Mater.* **2024**, *36*, 2307599.
- [34] Y. Su, X. Rong, H. Li, X. Huang, L. Chen, B. Liu, Y. S. Hu, *Adv. Mater.* **2023**, *35*, 2209402.
- [35] S. Jin, X. Shan, J. Tian, Y. Li, H. Ding, R. Advincula, M. Tian, P. F. Cao, *Adv. Funct. Mater.* **2025**, 2500440.
- [36] X. Hou, S. Chen, J. J. Koh, J. Kong, Y. W. Zhang, J. C. C. Yeo, H. Chen, C. He, *ACS Macro. Lett.* **2021**, *10*, 406.
- [37] J. W. Yeh, S. K. Chen, S. J. Lin, J. Y. Gan, T. S. Chin, T. T. Shun, C. H. Tsau, S. Y. Chang, *Adv. Eng. Mater.* **2004**, *6*, 299.
- [38] B. Cantor, I. T. H. Chang, P. Knight, A. J. B. Vincent, *Mater. Sci. Eng.: A* **2004**, *375–377*, 213.
- [39] C. M. Rost, E. Sachet, T. Borman, A. Moballegh, E. C. Dickey, D. Hou, J. L. Jones, S. Curtarolo, J. P. Maria, *Nat. Commun.* **2015**, *6*, 1.
- [40] A. Sarkar, L. Velasco, D. Wang, Q. Wang, G. Talasila, L. de Biasi, C. Kübel, T. Brezesinski, S. S. Bhattacharya, H. Hahn, B. Breitung, *Nat. Commun.* **2018**, *9*, 1.
- [41] X. Hou, Q. X. Pei, W. Sun, B. Song, H. Chen, Z. Liu, J. Kong, Y. W. Zhang, P. Liu, C. He, *Macromol. Rapid Commun.* **2024**, *45*, 2300543.
- [42] T. J. Whittle, G. J. Leggett, *Langmuir* **2009**, *25*, 2217.
- [43] F. Carrasco, P. Pagès, J. Gámez-Pérez, O. O. Santana, M. L. Maspoche, *Polym. Degrad. Stab.* **2010**, *95*, 116.
- [44] J. L. Olmedo-Martínez, L. Porcarelli, G. Guzmán-González, I. Calafel, M. Forsyth, D. Mecerreyres, A. J. Müller, *ACS Appl. Polym. Mater.* **2021**, *3*, 6326.
- [45] I. Osada, S. M. Hosseini, S. Jeong, S. Passerini, *ChemElectroChem* **2017**, *4*, 463.
- [46] N. Shukla, A. K. Thakur, *Springer* **2009**, *15*, 357.
- [47] A. Arya, A. L. Sharma, A. L. Sharma, *Ionics* **1908**, *23*, 497.
- [48] Y. Li, Z. Ni, J. Geng, Z. Wang, Y. Li, Y. Zhao, H. Shao, Y. Li, S. Xiong, J. Feng, *Adv. Energy Mater.* **2025**, *15*, 2502284.
- [49] M. Kerner, P. Johansson, *Batteries* **2018**, *4*, 10.
- [50] M. Wachowicz, J. L. White, *Macromolecules* **2007**, *40*, 5433.

- [51] P. J. Flory, *J. Chem. Phys.* **1942**, *10*, 51.
- [52] M. L. Huggins, *J. Chem. Phys.* **1941**, *9*, 440.
- [53] P. J. Flory, *Principles of Polymer Chemistry*, Cornell University Press, Ithaca, NY **1953**.
- [54] L. Mei, X. Wang, Y. Liu, J. Wang, *Mater. Sci.* **2019**, *25*, 54.
- [55] S. R. A. Karim, L. H. Sim, C. H. Chan, N. F. A. Zainal, A. K. Masitah, *Adv. Mat. Res.* **2013**, *812*, 267.
- [56] G. Huang, N. Wu, X. Wang, G. Zhang, L. Qiu, *Macromol. Rapid Commun.* **2022**, *43*, 2200149.
- [57] A. Takhulee, Y. Takahashi, V. Vao-soongnern, *J. Polym. Res.* **2017**, *24*, 1.
- [58] J. L. Olmedo-Martínez, L. Porcarelli, G. Guzmán-González, I. Calafel, M. Forsyth, D. Mecerreyres, A. J. Mü, *ACS Appl. Polym. Mater.* **2021**, *3*, 6326.
- [59] P. Saxena, P. Shukla, M. S. Gaur, *Polym. Polym. Compos.* **2021**, *29*, S11.
- [60] M. Muthuvinayagam, C. Gopinathan, *Polymer* **2015**, *68*, 122.
- [61] B. Metin, F. D. Blum, *J. Chem. Phys.* **2006**, *124*, 54908.
- [62] E. Y. Gómez-Pachón, R. Vera-Graziano, R. M. Campos, *IOP Conf. Ser.: Mater. Sci. Eng.* **2014**, *59*, 012003.
- [63] K. Matsuura, K. Kuboyama, T. Ougizawa, *Polym. Eng. Sci.* **2021**, *61*, 77.
- [64] T. Lin, Y. Li, J. Wang, J. You, *Polymers* **2021**, *13*, 4138.
- [65] A. Pawlak, *Crystals* **2024**, *14*, 385.
- [66] Z. Wang, M. Schaller, A. Petzold, K. Saalwächter, T. Thurn-Albrecht, *Proc. Natl. Acad. Sci.* **2023**, *120*, e2217363120.
- [67] L. Zhang, G. Zhao, G. Wang, *Polymers* **2021**, *13*, 3280.
- [68] J. H. Kim, A. Gadisa, C. Schaefer, H. Yao, B. R. Gautam, N. Balar, M. Ghasemi, I. Constantinou, F. So, B. T. O'Connor, K. Gundogdu, J. Hou, H. Ade, *J. Mater. Chem. A Mater.* **2017**, *5*, 13176.
- [69] S. K. Singh, P. Anthony, A. Chowdhury, *Orient. J. Chem.* **2018**, *34*, 1984.
- [70] S. Babo, J. L. Ferreira, A. M. Ramos, A. Micheluz, M. Pamplona, M. H. Casimiro, L. M. Ferreira, M. J. Melo, *Polymers* **2020**, *12*, 2198.
- [71] Y. Bao, S. Gao, W. Wang, D. Yu **2023**, <https://doi.org/10.2139/SSRN.4478539>.
- [72] M. Zhang, A. ling Zhang, Q. Li, F. fang Li, S. Wang, S. xi Li, *J. Polym. Environ.* **2019**, *27*, 2369.
- [73] A. K. Arof, S. Amirudin, S. Z. Yusof, I. M. Noor, *Phys. Chem. Chem. Phys.* **2014**, *16*, 1856.
- [74] K. Kim, L. Kuhn, I. V. Alabugin, D. T. Hallinan Jr., *Front. Energy Res.* **2020**, *8*, 569442.
- [75] K. M. Diederichsen, H. G. Buss, B. D. McCloskey, *Macromolecules* **2017**, *50*, 3831.
- [76] G. Y. Gu, R. Laura, K. M. Abraham, *Electrochim. Solid-State Lett.* **1999**, *2*, 486.
- [77] H. J. Rhoo, H. T. Kim, J. K. Park, T. S. Hwang, *Electrochim. Acta* **1997**, *42*, 1571.
- [78] V. Bocharova, A. P. Sokolov, *Macromolecules* **2020**, *53*, 4141.
- [79] K. Borutzki, D. Dong, C. Wölke, M. Kruteva, A. Stellhorn, M. Winter, D. Bedrov, G. Brunklaus, *iScience* **2020**, *23*, 101417.
- [80] N. S. Schausier, R. Seshadri, R. A. Segalman, *Mol. Syst. Des. Eng.* **2013**, *00*, 1.
- [81] W. W. Graessley, in *Advances in Polymer Science*, **1973**, *16*, Springer, Berlin, Heidelberg, <https://DOI:10.1007/BF0031037>.
- [82] Y. Zeng, B. Ouyang, J. Liu, Y. W. Byeon, Z. Cai, L. J. Miara, Y. Wang, G. Ceder, *Science* **2022**, *378*, 1320.
- [83] N. F. Mazuki, M. Z. Kufian, Y. Nagao, A. S. Samsudin, *J. Polym. Environ.* **2022**, *30*, 1864.
- [84] H. Zhang, Y. Wang, J. Huang, W. Li, X. Zeng, A. Jia, H. Peng, X. Zhang, W. Yang, *Energy Environ. Mater.* **2024**, *7*, e12514.
- [85] Y. Gao, N. Li, Y. Wu, W. Yang, S. H. Bo, *Adv. Energy Mater.* **2021**, *11*, 2100325.
- [86] Q. Wang, C. Zhao, J. Wang, Z. Yao, S. Wang, S. G. H. Kumar, S. Ganapathy, S. Eustace, X. Bai, B. Li, M. Wagemaker, *Nat. Commun.* **2023**, *14*, 1.
- [87] A. Bouzouita, PhD dissertation, Université de Mons, Valenciennes, France, and Mons, Belgium **2016**.
- [88] H. Doostmohammadi, M. Baniassadi, M. Bodaghi, M. Baghani, *Macromol. Mater. Eng.* **2024**, *309*, 2400090.
- [89] Y. Tong, B. M. Culbertson, *J. Macromol. Sci. Pure Appl. Chem.* **1998**, *35*, 1433.
- [90] N. Augustin, P. Muraliharan, A. Sabu, K. K. Senthilkumar, P. K. Annamalai, R. B. T. S. Raghava, *J. Thermoplast. Compos. Mater.* **2024**, *37*, 2527.
- [91] J. Mosa, J. F. Vélez, M. Aparicio, *Membranes* **2019**, *9*, 109.
- [92] A. Pawlak, J. Krajenta, *Molecules* **2024**, *29*, 3410.

Manuscript received: August 22, 2025

Revised manuscript received: October 6, 2025

Version of record online: